Spin coherence and echo modulation of the silicon vacancy in 4H-SiC at room temperature

S. G. Carter, Ö. O. Soykal, Pratibha Dev, Sophia E. Economou, and E. R. Glaser

Phys. Rev. B **92**, 161202 — Published 12 October 2015

DOI: 10.1103/PhysRevB.92.161202

Spin Coherence and Echo Modulation of the Silicon Vacancy in 4H-SiC at Room Temperature

S. G. Carter[1], Ö. O. Soykal[2], Pratibha Dev[2*], Sophia E. Economou[1†], E. R. Glaser[1]

[1] Naval Research Laboratory, Washington, DC 20375
[2] National Research Council Research Associate at the Naval Research Laboratory, Washington, DC 20375
[*] Present address: Department of Physics and Astronomy, Howard University, Washington, DC
[†] Present address: Department of Physics, Virginia Tech, Blacksburg, Virginia 24061

The silicon vacancy in silicon carbide is a strong emergent candidate for applications in quantum information processing and sensing. We perform room temperature optically-detected magnetic resonance and spin echo measurements on an ensemble of vacancies and find the spin echo properties depend strongly on magnetic field. The spin echo decay time varies from less than 10 μs at low fields to 80 μs at 68 mT, and a strong field-dependent spin echo modulation is also observed. The modulation is attributed to the interaction with nuclear spins and is well-described by a theoretical model.

Deep defect centers in solids are of great current interest as quantum bits or quantum emitters for applications in quantum computing, communication, and sensing, as they combine strengths from the solid state and the atomic world. In particular, the electronic and spin states of some defects have many desirable properties including high efficiency emission of single photons,[1–4] highly coherent spin states even at room temperature,[5–10] and optical initialization and readout.[11–13] Nitrogen-vacancy (NV) centers in diamond, consisting of a nitrogen atom substituted for a carbon next to a vacancy, have been extensively studied and have thus become the standard for such defects.

There is currently a strong interest to investigate similar defects in other material systems that may have improved properties for quantum applications. SiC has particularly attractive features, including significantly lower cost and mature microfabrication.[14–19] A number of defects in silicon carbide (SiC) have significant potential including the antisite-vacancy defect,[3,20] the Si vacancy,[10,12,13,21–33] and the divacancy.[7,9,34–36] Experiments have shown that some of these defects can have similar coherence and optical manipulation properties as NV centers.[7,10,12,36] The properties of these defects, however, are not as well-known as for the NV center, and there are several types of each defect that vary to some extent in the different polytypes of SiC.

The focus of this Rapid Communication is on the Si vacancy in SiC, a defect that has a distinct spin structure from other defects in SiC and NV centers and which as such may offer

additional capabilities.[28–30,32] Previous studies have established many of the optical and spin properties of this defect, including that it is observed negatively charged with S=3/2.[21,24–26,28] This defect allows for efficient optical spin initialization and readout[12,27] as well as coherent microwave manipulation.[12,24] Recently these capabilities have been demonstrated for an isolated vacancy, and the first spin echo measurements were performed, giving a decoherence time on the order of 100 μs at 27 and 28.8 mT.[10] However, very little is known of the spin coherence of this defect beyond this measurement. We perform optically-detected magnetic resonance (ODMR) and spin echo measurements on an ensemble of Si vacancies at room temperature. We carefully map out the ODMR as a function of magnetic field, providing a clearer picture of the spin transitions. We also perform the first magnetic field dependence of the spin coherence that reveals a strong dependence of the echo decay time on magnetic field and a strong echo modulation. These results agree very well with a detailed theoretical model that takes into account the unique spin structure and the hyperfine interaction with nearby nuclear spins.

Experiments are performed on high purity semi-insulating 4H-SiC. To generate Si vacancies, it is irradiated with 2 MeV electrons at a dose of 5×10^{17} cm^{-2}. Figure 1(b) displays the photoluminescence at low temperature (19 K) and room temperature. At low temperature there are several sharp lines, two of which at 1438 meV and 1353 meV have previously been identified as the zero-phonon lines (ZPL) of Si vacancies at the two inequivalent sites, labeled V1 and V2.[22] At room temperature, the emission consists of broadened ZPL and phonon sidebands from Si vacancies and likely emission from other defects.

ODMR measurements are performed at room temperature as illustrated in Fig. 1(a) by measuring changes in the PL when driving the system with a microwave magnetic field. The excitation laser is focused onto the sample with a 0.62 NA 50X objective that also collects PL and sends it to a Si photodiode. A microwave magnetic field is produced by shorting the inner conductor of a coax line to the outer conductor with a 50 μm diameter gold wire. The sample is oriented on its side in-between the poles of an electromagnet with B_{static} parallel to the c-axis.

The ODMR spectrum at 34 mT is displayed in Fig. 1(c) for three microwave powers, showing two strong lines separated by 140 MHz, which correspond to V2. There is no sign of V1 in the spectrum, consistent with other room temperature measurements.[10,28,29] The weaker pair of lines split by 70 MHz will be discussed later. The two strong lines are broadened at the highest microwave power, but at low powers each line is shown to be composed of three lines [see Fig. 1(d)]. The two weaker lines separated by 8 MHz correspond to vacancies with a next-nearest-neighbor (NNN) ^{29}Si nuclei (I=1/2), which shift the transition due to the hyperfine interaction.[23]

Figure 2(c) displays a map of ODMR as a function of both magnetic field and microwave frequency. At non-zero magnetic fields, there are clearly four transitions, with the stronger two having a slope corresponding to $\Delta m_s = \pm 1$ with g=2, and the weaker two having double the slope, corresponding to $\Delta m_s = \pm 2$. The presence of these four transitions with different slopes is a clear indication that this is a S=3/2 system instead of an S=1 system, which could have at most three

transitions. The spin Hamiltonian for this system is $H = g\mu_B \vec{B} \cdot \vec{S} + DS_z^2 + H_{hf}$, where $\vec{B}$ is the magnetic field vector, *z* is along the c-axis, *2D* is the zero-field splitting, and H_{hf} is the hyperfine interaction. The four calculated energy levels for S=3/2 are plotted as a function of B_z in Fig. 2(a). Only $\Delta m_s = \pm 1$ transitions are magnetic dipole allowed, suggesting that only $-3/2 \rightarrow -1/2$, $+1/2 \rightarrow +3/2$, and $-1/2 \rightarrow +1/2$ should occur (labeled *a*, *b,* and *c*, respectively), but mixing due to a stray B-field perpendicular to the c-axis or the hyperfine interaction allows weak $\Delta m_s = \pm 2$ transitions, $-3/2 \rightarrow +1/2$ and $-1/2 \rightarrow +3/2$ (labeled *d* and *e*). While transition *c* is allowed, it does not appear in the spectrum because of the mechanism for ODMR, in which spin-dependent processes are only selective between the $m_s = \pm 1/2$ and $\pm 3/2$ states.[27,28,37]

Figure 2(d) displays model calculations of the ODMR, with good qualitative agreement with experiment.[37] A level anticrossing (LAC) between $m_s = -1/2$ and $-3/2$ is apparent at 2.5 mT, which strongly reduces the ODMR signal. The strength of the LAC is determined by mixing induced by a magnetic field perpendicular to the c-axis. A perpendicular field of 0.05 mT is included, estimating the average field from NNN ^{29}Si nuclei. In Fig. 2(e) the strength of the ODMR lines *a* and *b* are plotted as a function of magnetic field, illustrating the intensity dip at 2.5 mT and a weaker, broader dip at 16 mT that we assign to a LAC of ES spin levels. At fields far above the GS LAC [as in Fig. 1(c)], only transitions *a* and *b* remain with a splitting of 4D=140 MHz. At high microwave power, two-photon versions of transitions *d* and *e* are also present in Fig. 1(c),[28] with a splitting of 2D = 70 MHz.

We have also performed Hahn spin echo measurements to eliminate the effects of inhomogeneous broadening and slow variations in the environment. The sequence in Fig. 3(a) consists of a NIR pulse of 2 μs to polarize and read-out the spins simultaneously, followed by three microwave pulses with lengths designed to give a $\pi/2$-π-$\pi/2$ sequence. The microwave pulse lengths were determined by measuring Rabi oscillations with a single microwave pulse of variable length, as plotted in Fig. 3(b). The oscillations are heavily damped, due to the relatively short inhomogeneous dephasing time T_2^*.

The spin echo measurements at 34 mT in Fig. 3(c,d) are obtained by setting the microwave frequency to transition *b*, and scanning *t*, the third pulse delay relative to the first pulse, for a series of delays *T* of the π-pulse (2^{nd} pulse). In Fig. 3(c) the spin echo is displayed for T = 1 μs, which appears as a sharp dip at 2 μs with rapidly decaying oscillations at a frequency of 4.1 MHz. The oscillations are consistent with the hyperfine splitting that gives three different transition frequencies beating with each other. The decay time of 190 ns corresponds to T_2^*, consistent with the low power transition linewidth.

In Fig. 3(d), the echo amplitude appears to oscillate with T without clear decay. To better study this behavior we display the amplitude of the echo as a function of T for a series of magnetic fields in Fig. 4(a-e), going out to T = 30 μs. There is clearly echo modulation at all

these fields. The oscillations do not have a single frequency, but the modulation timescales are comparable to the Zeeman precession periods of ^{13}C and ^{29}Si. (The nuclear Zeeman periods are $2\pi/\omega_{Si}$ = 11.8 μs and $2\pi/\omega_C$ = 9.35 μs at 10 mT.) The modulation amplitude also appears to decrease at the highest field. There is little decay of the echo at 68 mT on this time scale, so we also measured the echo amplitude out to T = 55 μs in Fig. 4(f). From an exponential fit, the echo decay time is 81±4 μs, similar to the value obtained in Ref. 10 for a single Si vacancy. Clearly the decay is much faster for fields lower than 20 mT despite weak revivals at longer delays, falling below $1/e$ of the maximum by T = 3-4 μs.

The spin echo data shows Electron Spin Echo Envelope Modulation[38,39] that results from the anisotropic spin-spin interactions between the unpaired electrons in the vacancy and nearby nuclei. We theoretically describe this behavior with the following spin Hamiltonian: $H = g\mu_B BS_z + DS_z^2 + \omega_I I_z + S_z A I_z + S_z A' I_x + \Omega S_x$, where z is along the c-axis. The magnetic field is oriented along the c-axis, Ω is the Rabi frequency from the microwave drive field, and both nuclear species with non-zero spin, ^{29}Si and ^{13}C (both I = ½), are considered. The A-term in the Hamiltonian contains contributions from the isotropic (Fermi contact interaction) and anisotropic dipole-dipole hyperfine interaction. A' is the pseudosecular contribution from the anisotropic hyperfine interaction. Both A and A' depend on the vacancy-nucleus distance and the orientation of the pair with respect to the c-axis. Due to the A' term, the quantization axis of the nuclear spin is not aligned along z and changes with the spin state of the vacancy. Nuclear spin precession thus results in a time-varying effective magnetic field for the electron spin. This results in imperfect rephasing when there is significant nuclear precession during time T. Even though all four levels of m_s=±3/2, ±1/2 are included in our calculations, consideration of only the directly driven m_s= +1/2 and +3/2 states can be used to obtain a simplified analytical form for the echo signal from a single nuclear site that is proportional to $1-\frac{2\omega_I^2 A'^2}{\omega_{3/2}^2\omega_{1/2}^2}\sin^2\frac{\omega_{3/2}\tau}{2}\sin^2\frac{\omega_{1/2}\tau}{2}$, where $\omega_{j=1/2,3/2} = \sqrt{(\omega_I + jA)^2 + (jA')^2}$ are the nuclear precession frequencies when the electronic system is in the m_s= +1/2 or +3/2 state. This mechanism for echo modulation appears to have essentially the same origin as that observed for NV centers in diamond,[40,41] with the exception that there is no m_s = 0 state in which the hyperfine interaction is absent. The modulation frequency is always sensitive to the strength of the hyperfine interaction here. In turn, the hyperfine interaction, being dependent on the position of the nuclear spins, gives rise to many different modulation frequencies. In this work, we obtain the fully relaxed positions of Si and C atoms around the defect from the density functional theory calculation. We then calculate the echo signal from all possible configurations for any number of ^{29}Si and ^{13}C within a ~10 Å radius centered on the vacancy. Each configuration is weighted according to their probabilities, determined by the natural abundances of 4.7% and 1.1%, respectively.[37] We treat multiple nuclear spins interacting with a single vacancy independently,[38,42] since the nuclear spin-spin interactions are negligible at these timescales. The modulation is largest for nuclear sites far

enough away from the vacancy such that the dipole-dipole interaction dominates (*i.e*. beyond NNN at 3.08 Å) over the Fermi contact, but close enough to have a significant hyperfine interaction (*i.e*. within ~10 Å).

The theoretical spin echo is plotted with the experimental data in Fig. 4(a-f) with very good agreement, considering the complexity of the nuclear spin environment and the fact that there are no adjustable parameters in the theory. The timescales of the modulation match the experiment well, along with the trend of rapid echo decay at low fields. The discrepancies in the phase and frequency of the modulation could be due to subtle differences in the hyperfine interaction or the presence of other impurities not accounted for in the theory. There is no decoherence included in the theory, so this decay is the result of interfering modulation frequencies that rapidly reduce the echo amplitude.[31] Thus, the measured echo decay time provides a lower limit on the true coherence time, T_2. As the magnetic field increases, the echo modulation amplitude decreases as the ratio A'/ω_I decreases, leading to less initial decay. At these higher fields the nuclear quantization axis approaches the electron spin quantization axis, resulting in no modulation of the electron spin frequency. This behavior does not seem as noticeable for S=1 systems such as the NV center in diamond where nuclear precession in the m_s= 0 state is fixed. The longer timescale decay and weak revival in the theoretical echo in Fig. 4(f) only occur whent the m_s= −1/2 and −3/2 states are included in the theory. Further studies should be performed to test for this revival and decay behavior at longer delays and better understand the physical mechanism.

The results presented in this Rapid Communication provide important advances in understanding the spin properties of the Si vacancy that will be essential to assessing how it may be used for quantum applications. The mapping of the ODMR transitions as a function of magnetic field gives a clearer picture of the different possible transitions and how they can arise in a S=3/2 system. We also present the first ensemble spin echo measurements in this system that show significant echo modulation and a fast decay at low magnetic fields attributed to interference between many nuclear spin configurations with different modulation frequencies. This modulation and decay behavior is reproduced very well by a theoretical model with no fitting parameters that considers all of the possible nuclear spin configurations. At higher magnetic fields, the spin echo decay time is 80 μs, comparable to initial spin echo measurements of NV centers in diamond[5,40] and of single Si vacancies,[10] which is a further indication of the utility of the SiC platform for quantum technologies.

This work is supported by the U.S. Office of Naval Research and in part by the Defense Threat Reduction Agency, Basic Research Award #HDTRA1-15-1-0011. Computer resources were provided by the DoD High Performance Computing Modernization Program. O.S. and P.D. acknowledge the NRL-NRC Research Associateship Program.

[1] C. Kurtsiefer, S. Mayer, P. Zarda, and H. Weinfurter, Phys. Rev. Lett. **85**, 290 (2000).

[2] I. Aharonovich, S. Castelletto, D.A. Simpson, A. Stacey, J. McCallum, A.D. Greentree, and S. Prawer, Nano Lett. **9**, 3191 (2009).
[3] S. Castelletto, B.C. Johnson, V. Ivády, N. Stavrias, T. Umeda, A. Gali, and T. Ohshima, Nat. Mater. **13**, 151 (2014).
[4] L.J. Rogers, K.D. Jahnke, T. Teraji, L. Marseglia, C. Müller, B. Naydenov, H. Schauffert, C. Kranz, J. Isoya, L.P. McGuinness, and F. Jelezko, Nat. Commun. **5**, 4739 (2014).
[5] T.A. Kennedy, J.S. Colton, J.E. Butler, R.C. Linares, and P.J. Doering, Appl. Phys. Lett. **83**, 4190 (2003).
[6] G. Balasubramanian, P. Neumann, D. Twitchen, M. Markham, R. Kolesov, N. Mizuochi, J. Isoya, J. Achard, J. Beck, J. Tissler, V. Jacques, P.R. Hemmer, F. Jelezko, and J. Wrachtrup, Nat. Mater. **8**, 383 (2009).
[7] W.F. Koehl, B.B. Buckley, F.J. Heremans, G. Calusine, and D.D. Awschalom, Nature **479**, 84 (2011).
[8] N. Bar-Gill, L.M. Pham, A. Jarmola, D. Budker, and R.L. Walsworth, Nat. Commun. **4**, 1743 (2013).
[9] A.L. Falk, B.B. Buckley, G. Calusine, W.F. Koehl, V. V Dobrovitski, A. Politi, C.A. Zorman, P.X.-L. Feng, and D.D. Awschalom, Nat. Commun. **4**, 1819 (2013).
[10] M. Widmann, S.-Y. Lee, T. Rendler, N.T. Son, H. Fedder, S. Paik, L.-P. Yang, N. Zhao, S. Yang, I. Booker, A. Denisenko, M. Jamali, S.A. Momenzadeh, I. Gerhardt, T. Ohshima, A. Gali, E. Janzén, and J. Wrachtrup, Nat. Mater. **14**, 164 (2015).
[11] N.B. Manson, J.P. Harrison, and M.J. Sellars, Phys. Rev. B **74**, 104303 (2006).
[12] V.A. Soltamov, A.A. Soltamova, P.G. Baranov, and I.I. Proskuryakov, Phys. Rev. Lett. **108**, 226402 (2012).
[13] D. Riedel, F. Fuchs, H. Kraus, S. Väth, A. Sperlich, V. Dyakonov, A.A. Soltamova, P.G. Baranov, V.A. Ilyin, and G. V. Astakhov, Phys. Rev. Lett. **109**, 226402 (2012).
[14] Y.T. Yang, K.L. Ekinci, X.M.H. Huang, L.M. Schiavone, M.L. Roukes, C.A. Zorman, and M. Mehregany, Appl. Phys. Lett. **78**, 162 (2001).
[15] B.-S. Song, S. Yamada, T. Asano, and S. Noda, Opt. Express **19**, 11084 (2011).
[16] J. Cardenas, M. Zhang, C.T. Phare, Y. Shreyas, C.B. Poitras, B. Guha, and M. Lipson, Opt. Express **21**, 16882 (2013).
[17] R. Maboudian, C. Carraro, D.G. Senesky, and C.S. Roper, J. Vac. Sci. Technol. A Vacuum, Surfaces, Film. **31**, 050805 (2013).
[18] J.D. Caldwell, O.J. Glembocki, Y. Francescato, N. Sharac, V. Giannini, F.J. Bezares, J.P. Long, J.C. Owrutsky, I. Vurgaftman, J.G. Tischler, V.D. Wheeler, N.D. Bassim, L.M. Shirey, R. Kasica, and S.A. Maier, Nano Lett. **13**, 3690 (2013).
[19] G. Calusine, A. Politi, and D.D. Awschalom, Appl. Phys. Lett. **105**, 011123 (2014).
[20] W.E. Carlos, E.R. Glaser, and B. V. Shanabrook, Phys. B **340-342**, 151 (2003).
[21] T. Wimbauer, B.K. Meyer, A. Hofstaetter, A. Scharmann, and H. Overhof, Phys. Rev. B **56**, 7384 (1997).
[22] E. Sorman, N.T. Son, W.M. Chen, O. Kordina, C. Hallin, and E. Janzen, Phys. Rev. B **61**, 2613 (2000).
[23] M. Wagner, N.Q. Thinh, N.T. Son, W.M. Chen, E. Janzén, P.G. Baranov, E.N. Mokhov, C. Hallin, and J.L. Lindström, Phys. Rev. B **66**, 155214 (2002).
[24] N. Mizuochi, S. Yamasaki, H. Takizawa, N. Morishita, T. Ohshima, H. Itoh, and J. Isoya, Phys. Rev. B **66**, 235202 (2002).

[25] N. Mizuochi, S. Yamasaki, H. Takizawa, N. Morishita, T. Ohshima, H. Itoh, and J. Isoya, Phys. Rev. B **68**, 165206 (2003).
[26] J. Isoya, T. Umeda, N. Mizuochi, N.T. Son, E. Janzén, and T. Ohshima, Phys. Status Solidi **245**, 1298 (2008).
[27] P.G. Baranov, A.P. Bundakova, A.A. Soltamova, S.B. Orlinskii, I. V. Borovykh, R. Zondervan, R. Verberk, and J. Schmidt, Phys. Rev. B **83**, 125203 (2011).
[28] H. Kraus, V.A. Soltamov, D. Riedel, S. Väth, F. Fuchs, A. Sperlich, P.G. Baranov, V. Dyakonov, and G. V. Astakhov, Nat. Phys. **10**, 157 (2014).
[29] H. Kraus, V.A. Soltamov, F. Fuchs, D. Simin, A. Sperlich, P.G. Baranov, G. V Astakhov, and V. Dyakonov, Sci. Rep. **4**, 5303 (2014).
[30] A. Muzha, F. Fuchs, N. V. Tarakina, D. Simin, M. Trupke, V.A. Soltamov, E.N. Mokhov, P.G. Baranov, V. Dyakonov, A. Krueger, and G. V. Astakhov, Appl. Phys. Lett. **105**, 243112 (2014).
[31] L.-P. Yang, C. Burk, M. Widmann, S.-Y. Lee, J. Wrachtrup, and N. Zhao, Phys. Rev. B **90**, 241203 (2014).
[32] D. Simin, F. Fuchs, H. Kraus, A. Sperlich, P.G. Baranov, G. V. Astakhov, and V. Dyakonov, Phys. Rev. Appl. **4**, 014009 (2015).
[33] Ö.O. Soykal, P. Dev, and S.E. Economou, arXiv:1507.05091 (2015).
[34] N.T. Son, P. Carlsson, J. ul Hassan, E. Janzén, T. Umeda, J. Isoya, A. Gali, M. Bockstedte, N. Morishita, T. Ohshima, and H. Itoh, Phys. Rev. Lett. **96**, 055501 (2006).
[35] W.E. Carlos, N.Y. Garces, E.R. Glaser, and M.A. Fanton, Phys. Rev. B **74**, 235201 (2006).
[36] D.J. Christle, A.L. Falk, P. Andrich, P. V Klimov, J. Ul Hassan, N.T. Son, E. Janzén, T. Ohshima, and D.D. Awschalom, Nat. Mater. **14**, 160 (2015).
[37] See supplemental Material at [] for details on the experiments, ODMR model calculations, the spin echo theory, and additional ODMR data.
[38] L.G. Rowan, E.L. Hahn, and W.B. Mims, Phys. Rev. **137**, A61 (1965).
[39] S.A. Dikanov and Y. Tsvetkov, *Electron Spin Echo Envelope Modulation (ESEEM) Spectroscopy* (CRC Press, Boca Raton, FL, 1992).
[40] E. Van Oort and M. Glasbeek, Chem. Phys. **143**, 131 (1990).
[41] L. Childress, M.V.G. Dutt, J.M. Taylor, A.S. Zibrov, F. Jelezko, J. Wrachtrup, P.R. Hemmer, and M.D. Lukin, Science **314**, 281 (2006).
[42] W.B. Mims, Phys. Rev. B **5**, 2409 (1972).

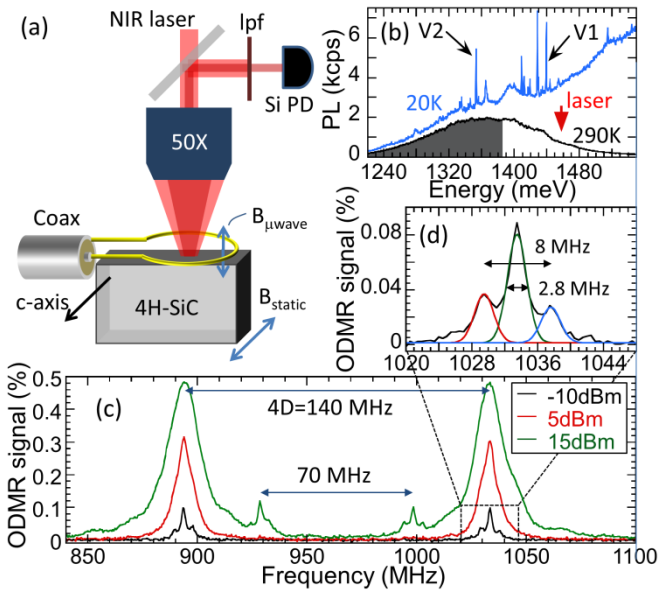

FIG. 1 (color online). (a) Experimental setup for optically-detected magnetic resonance (ODMR). The scattered laser light is filtered from the photoluminescence (PL) by a long pass filter (lpf) and sent to a silicon photodiode (Si PD). (b) PL at 20 K and 290 K, exciting at 532 nm, with 290 K PL scaled down by a factor of 2 for clarity. The typical lpf collection range is shaded in grey, and the typical laser energy is indicated with a vertical arrow. (c) ODMR spectra for B = 34 mT || c-axis for a series of microwave powers. The vertical scale is the percent change in PL. (d) ODMR at -10 dBm from (c) with the scale expanded to show the hyperfine splitting. Individual Gaussian functions of a three-peak fit are plotted with the spectrum.

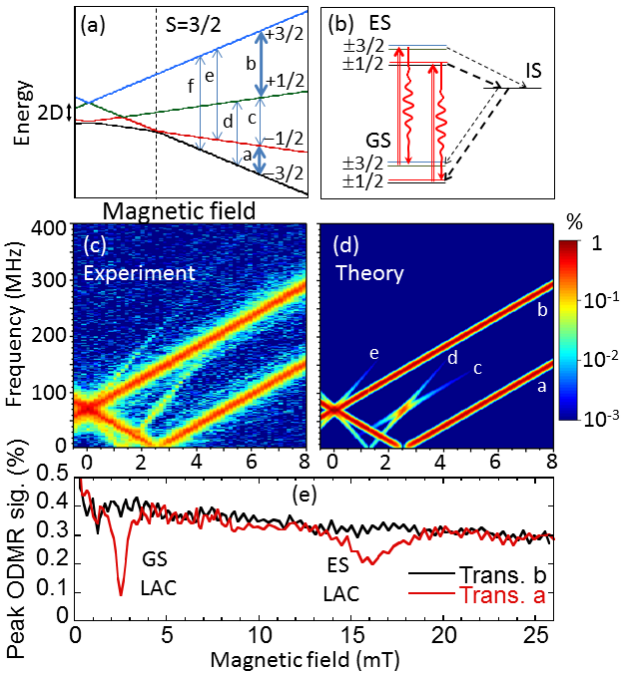

FIG. 2 (color online). (a) Energy levels of the S=3/2 spin states as a function of magnetic field parallel to the c-axis. (b) Energy level diagram showing optical excitation and emission between the ground states (GS) and the excited states (ES), along with relaxation to the intermediate states (IS) that result in GS spin polarization. (c) ODMR map as a function of microwave frequency and magnetic field (parallel to the c-axis). The color scale mapping of the ODMR signal is logarithmic as displayed by the color bar right of (d). (d) Model calculations of the ODMR with a weak perpendicular magnetic field of 0.05 mT. The model signal maximum has been scaled to match the experimental maximum, using the same color bar. (e) ODMR amplitude for transitions *a* and *b* as a function of the magnetic field.

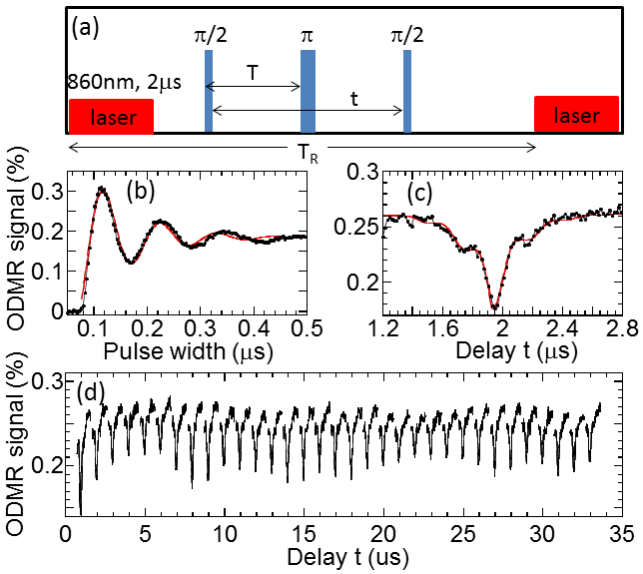

FIG. 3 (color online). (a) Hahn echo sequence with repetition period T_R. Narrow blue rectangles represent microwave pulses, and the shorter red rectangles represent laser pulses. (b) Microwave Rabi oscillations with only a single microwave pulse in the sequence, with T_R = 10 μs. The red line is a fit to an exponentially decaying cosine (c) Spin echo with T_R = 40 μs and T = 1 μs. The red line is a fit to $-\exp\left(-\left|t-2T\right|/T_2^*\right)$ modulated by a cosine. (d) Spin echo as a function of *t* for a series of values of *T*, with T_R = 40 μs. The echo appears at t = 2T. All measurements in (b,c,d) are at room temperature with a magnetic field of 34 mT parallel to the c-axis and a microwave power of 20 dBm.

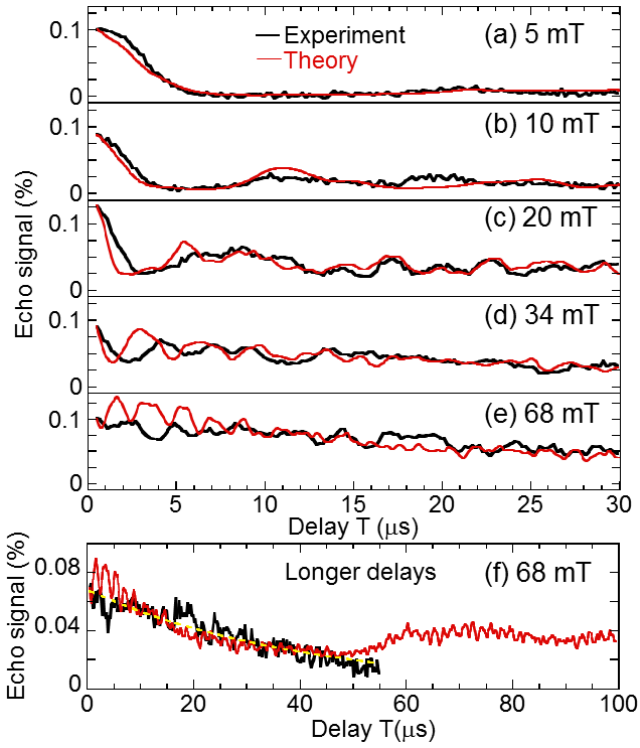

FIG. 4 (color online). (a-e) Experimental and theoretical echo signal as a function of T for a series of magnetic fields parallel to the c-axis, with T_R = 66.7 μs. The experimental echo signal is obtained by taking the difference between the ODMR signal at t = 2T + 0.8 μs and t = 2T, and the theory is normalized to best match the experimental data. (f) Echo as a function of T at B = 68 mT and T_R = 125 μs, with an exponential fit shown as a dashed line. All measurements are at room temperature.